ACS NANO
Cite This: ACS Nano 2017, 11, 12210–12218
www.acsnano.org

ARTICLE

Enzyme-Mimetic Antioxidant Luminescent Nanoparticles for Highly Sensitive Hydrogen Peroxide Biosensing

Anna Pratsinis,[†] Georgios A. Kelesidis,[‡] Stefanie Zuercher,[†] Frank Krumeich,[‡] Sreenath Bolisetty,[∥] Raffaele Mezzenga,[∥] Jean-Christophe Leroux,[†] and Georgios A. Sotiriou*[,†,§]

[†]Drug Formulation and Delivery, Institute of Pharmaceutical Sciences, Department of Chemistry and Applied Biosciences, ETH Zurich, 8093 Zurich, Switzerland

[‡]Particle Technology Laboratory, Institute of Process Engineering, Department of Mechanical and Process Engineering, ETH Zurich, 8092 Zurich, Switzerland

[∥]Food and Soft Materials, Institute of Food, Nutrition and Health, Department of Health Sciences and Technology, ETH Zurich, 8092 Zurich, Switzerland

[§]Department of Microbiology, Tumor and Cell Biology, Karolinska Institutet, 17177 Stockholm, Sweden

Supporting Information

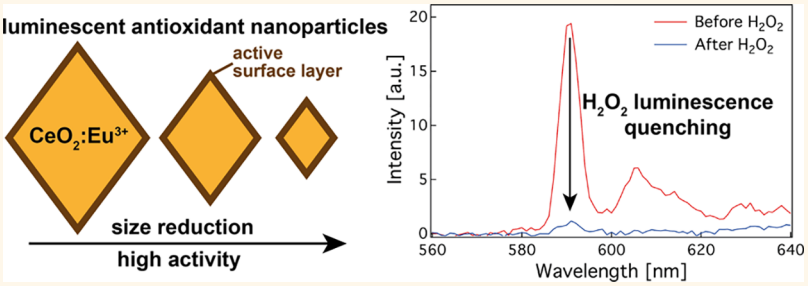

ABSTRACT: Hydrogen peroxide (H_2O_2) is an abundant molecule associated with biological functions and reacts with natural enzymes, such as catalase. Even though direct H_2O_2 measurement can be used to diagnose pathological conditions, such as infection and inflammation, H_2O_2 quantification further enables the detection of disease biomarkers in enzyme-linked assays (*e.g.*, ELISA) in which enzymatic reactions may generate or consume H_2O_2. Such a quantification is often measured optically with organic dyes in biological media that suffer, however, from poor stability. Currently, the optical H_2O_2 biosensing without organic-dyes in biological media and at low, submicromolar, concentrations has yet to be achieved. Herein, we rationally design biomimetic artificial enzymes based on antioxidant CeO_2 nanoparticles that become luminescent upon their Eu^{3+} doping. We vary systematically their diameter from 4 to 16 nm and study their catalase-mimetic antioxidant activity, manifested as catalytic H_2O_2 decomposition in aqueous solutions, revealing a strong nanoparticle surface area dependency. The interaction with H_2O_2 influences distinctly the particle luminescence rendering them highly sensitive H_2O_2 biosensors down to 0.15 μM (5.2 ppb) in solutions for biological assays. Our results link two, so far, unrelated research domains, the CeO_2 nanoparticle antioxidant activity and luminescence by rare-earth doping. When these enzyme-mimetic nanoparticles are coupled with alcohol oxidase, biosensing can be extended to ethanol exemplifying how their detection potential can be broadened to additional biologically relevant metabolites. The enzyme-mimetic nanomaterial developed here could serve as a starting point of sophisticated *in vitro* assays toward the highly sensitive detection of disease biomarkers.

KEYWORDS: *nanozyme, biomimetic, cerium oxide, biosensor, rare-earth doping*

Hydrogen peroxide (H_2O_2) is present in numerous biological processes, and is the most stable and abundant reactive oxygen species (ROS) *in vivo*.[1] It can be generated during infection and inflammation,[2] and is typically decomposed by the enzyme catalase (CAT).[3] There is a large interest in H_2O_2 biosensing, not only as a potential biomarker for infections or inflammation, but also as an intermediate biomolecule in analytical assays coupled with

Received: August 3, 2017
Accepted: November 21, 2017
Published: November 28, 2017

DOI: 10.1021/acsnano.7b05518
ACS Nano 2017, 11, 12210–12218

enzymes that either consume or generate H_2O_2. For example, H_2O_2 is sensed in CAT-based assays for the ultrasensitive detection of HIV biomarker (capsid antigen p24)[4] and in assays employing the oxidase enzymes to monitor glycemia[5,6] or ethanol levels.[7] While H_2O_2 may be detected by highly sensitive electrochemical analytical assays,[8] typical commercial assays for the optical detection of H_2O_2 employ organic dyes in peroxidase-coupled reactions.[6] However, such reagents suffer from poor stability in ambient conditions (*e.g.*, room lighting) and require tedious procedures.[9] Therefore, the development of optically based, enzyme-, conjugate-, and label-free H_2O_2 biosensors with submicromolar limit-of-detection (LOD) is highly desired though yet to be achieved.[5,9−15] Even though high concentrations of H_2O_2 ($\geq$10 μM) are required to induce cell death (*e.g.*, infection or inflammation) for example as a host defense mechanism,[16] H_2O_2 biosensors with submicromolar LOD would be valuable in enzyme-linked assays in which H_2O_2 is a product of an enzymatic reaction linked to the presence of specific disease biomarkers enabling their detection at low concentrations toward the early diagnosis of diseases.[4]

Recently, several nanomaterials have been shown to exhibit enzyme-like properties, the so-called nanozymes,[17] owing to their redox potential.[18] One of the most studied enzyme-like nanomaterials is CeO_2 that has displayed regenerated ROS-scavenging[19,20] mediated by superoxide dismutase (SOD)- and CAT-mimetic activity.[1,21] The SOD-mimetic activity is generally attributed to the oxidation of Ce surface atoms (Ce^{3+} to Ce^{4+}).[22] The underlying mechanism of CAT-mimetic activity, which is usually expressed as the catalytic decomposition of H_2O_2, has been ascribed to the adsorption of oxygen species on active surface sites (*e.g.*, oxygen vacancies) on the nanoparticle surface.[23,24] This way, CeO_2 nanoparticles act as electron sponges upon H_2O_2 decomposition increasing their coordination number (Ce−O bond length) with a delocalized charge density redistribution over the entire nanoparticle.[25] Other nanomaterials with surface defects may also exhibit enzyme-mimetic H_2O_2 decomposition.[8,26] Nanoceria particles have demonstrated effective *in vitro* and *in vivo* ROS-scavenging by preventing ROS-mediated cell death in rat retina,[27] spinal cord neurons,[28] and keratinocytes.[29] Furthermore, the unique redox properties of these nanomaterials have been exploited for the development of enzyme-free H_2O_2 sensors.[8,30,31]

In the present study, we rationally design a highly sensitive, label-free H_2O_2 biosensor based on enzyme-mimetic CeO_2 nanoparticles doped with Eu^{3+} that renders them luminescent. We fabricate CeO_2:Eu^{3+} nanoparticles by flame spray pyrolysis (FSP), a highly scalable and reproducible process,[32] and systematically vary the average nanoparticle crystal size from 4 to 16 nm to establish whether their antioxidant activity, expressed as their CAT-mimetic decomposition of H_2O_2, is attributed to the surface concentration. During this reaction, the strong interaction of oxygen species with the active sites (*e.g.*, oxygen vacancies) of the CeO_2 nanoparticle surface markedly quenches the luminescence of these nanoparticles, rendering them superior submicromolar H_2O_2 sensors in biological media. The size-dependent luminescence quenching and enzyme-like antioxidant properties of CeO_2 nanoparticles strongly link the enzyme-like activity to the particle surface.[23,25] In a final step, the potential of these enzyme-mimetic nanoparticles to detect alcohol is verified in an alcohol oxidase (AOx) coupled reaction. This provides the framework for the employment of such luminescent enzyme-mimetic nanoparticles as H_2O_2 biosensors, which can be extended to additional biologically relevant metabolites when linked to a corresponding reaction.

RESULTS AND DISCUSSION

Nanoparticle Morphology. The size of flame-made CeO_2:Eu^{3+} (5 at%) nanoparticles can be finely controlled by the synthesis process conditions, and more specifically by the precursor concentration in the gas phase.[33] The high control over the nanoparticle size can be validated by the X-ray diffraction (XRD) patterns of five CeO_2:Eu^{3+} nanoparticles prepared at increasing precursor concentrations, as illustrated in Figure 1a. All patterns exhibit the characteristic CeO_2 cubic crystal structure (inverse triangles, ICDS: 061595) without any Eu-oxide peaks, indicating successful incorporation of the Eu^{3+} ions within the crystal host matrix.[34] The XRD peaks sharpen for increasing precursor concentration indicating larger crystal sizes.[33] In fact, the average crystal diameter d_{XRD} calculated by Rietveld analysis of these patterns is plotted in Figure 1b (black triangles, left ordinate) as a function of the precursor concentration along with the measured specific surface area (SSA, red diamonds, right ordinate), as determined from N_2 adsorption. The average crystal diameter monotonically increases for higher precursor concentrations (d_{XRD} = 4.4 to 15.8 nm), highlighting the precise control over the average nanoparticle size with this manufacture process. Figure 1c−g shows representative high-resolution transmission electron microscopy (TEM) images of all nanocrystals for increasing precursor concentration. The particle size distributions derived from TEM analysis are shown in the Supporting Information in Figure S1 (d_{TEM} = 5.1 to 13.0 nm, σ_g = 1.27 to 1.56 for all the samples here) and agree well with the average primary particle size determined by XRD, indicating the formation of monocrystalline nanoparticles. The average d_{BET} of all samples here calculated by the measured SSA is consistently lower (d_{BET}= 2.9 to 9.1 nm) than the average d_{XRD} and d_{TEM} and in agreement with the literature.[33] This is probably due to the primary particle shape and polydispersity and thus BET might not be the most accurate measurement for these nonspherical nanoparticles, as the d_{BET} assumes spherical monodisperse particles. Even though for the smallest nanoparticles their shape appears rather irregular, for larger sizes the particles exhibit the characteristic rhomboidal shape of flame-made CeO_2 nanoparticles (Supporting Information for further TEM images, Figure S2)[33] indicating that the incorporation of Eu^{3+} in the crystal lattice has little influence on the morphology of such nanoparticles (crystals encircled in red dotted lines for clarity). Upon dispersion by ultrasonication of these particles in aqueous solutions, they form large agglomerates independent of their primary particle size[35−37] (Supporting Information, Table S1) due to their isoelectric point (pH 6.7 to 7.5).[36] The hydrodynamic diameter (Supporting Information, Table S1) and zeta potential agree well with the literature for similar samples.[35−37]

The incorporation of the Eu^{3+} ions within the CeO_2 crystal matrix renders these particles luminescent.[38] Figure 1h shows the excitation (dotted lines, emission wavelength λ = 590 nm) and emission spectra (solid lines, excitation wavelength λ = 330 nm) of all CeO_2:Eu^{3+} nanoparticles measured in dry form after slight compaction into pellets. The samples exhibit the characteristic emission peaks attributed to Eu^{3+} assigned to various $^5D_0$-^7F_J transitions,[38,39] with the dominant one around 590 nm corresponding to the magnetic dipole allowing transition $^5D_0$-$^7F_1$, thereby indicating high inversion symmetry

DOI: 10.1021/acsnano.7b05518
ACS Nano 2017, 11, 12210−12218

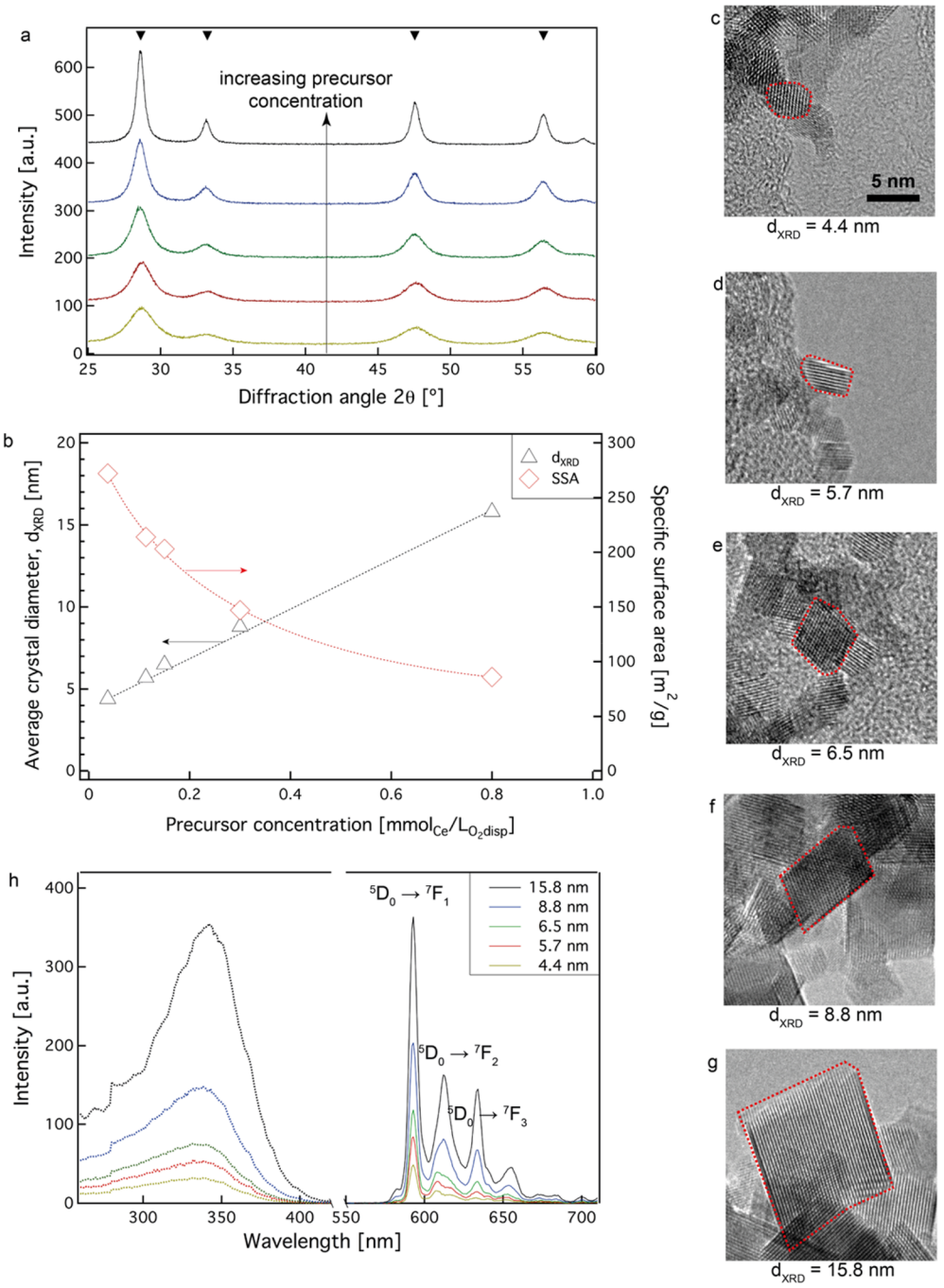

Figure 1. Physicochemical and morphological characterization of CeO_2:Eu^{3+} nanoparticles. (a) XRD patterns of all CeO_2:Eu^{3+} nanoparticles prepared at different precursor concentration (feed rate of precursor solution/feed rate of O_2 dispersion gas). The characteristic CeO_2 peaks (ICDS 061595, inverse triangles) sharpen for increasing precursor concentration indicating larger crystal sizes. (b) Average crystal diameter as determined by XRD (d_{XRD}, triangles, left ordinate) and specific surface area as measured by N_2 adsorption (SSA, red diamonds, right ordinate) as a function of precursor concentration. Larger particles are obtained for increasing precursor concentrations. (c–g) High-resolution TEM images of selected samples. The scale bar of 5 nm is identical for all images. (h) Excitation (dotted lines) and emission spectra (solid lines) of all CeO_2:Eu^{3+} nanoparticles measured in the dry form that exhibit the characteristic Eu^{3+} emission peaks with increasing intensities for larger sizes.

in the CeO_2:Eu^{3+} nanocrystals.[39] All excitation spectra (Figure 1h, dotted lines) appear as rather broad bands, which can be ascribed to the Ce–O charge transfer (from the O^{2-} to Ce^{4+}).[38] The emission intensity strongly depends on the average nanoparticle size with higher intensities for larger crystal sizes (Supporting Information, Figure S3), in agreement with the literature for similar flame-made rare-earth doped nanocrystals.[40] Small nanoparticles have a higher surface defect concentration than large nanoparticles, offering more non-radiative transfer routes.[39]

Catalase-Mimetic Activity for H_2O_2 Decomposition. Flame aerosol nanomanufacture is a high-temperature atmospheric (O_2-rich) process resulting in CeO_2 nanoparticles with negligible surface Ce^{3+} contents (see X-ray photoelectron spectroscopy data in Supporting Information, Figure S4), which behave similar to CAT by decomposing H_2O_2 in solution.[41]

DOI: 10.1021/acsnano.7b05518
ACS Nano 2017, 11, 12210–12218

Figure 2a shows the CAT-mimetic activity of all CeO_2:Eu^{3+} nanoparticles at the same mass concentration (1.25 g/L, open symbols) by following the H_2O_2 concentration (initial concentration = 50 mM) over time. As negative and positive controls, pure water (blue pentagons) and CAT (0.5 mg/L, red diamonds) are added, respectively. While all nanoparticles exhibit CAT-mimetic activity, there is a clear size-dependency with the smallest ones being the most active, suggesting a surface area dependency. In fact, when the CAT-mimetic activity (decomposed H_2O_2 after 1 h) is plotted in Figure 2b as a function of surface area concentration, data obtained after 1 h from Figure 2a (open symbols) follow the same trend (dashed line). A statistically significant difference between the H_2O_2 scavenging measured after 1 h at the same mass concentration could be established among all assayed CeO_2:Eu^{3+} nanoparticles with the exception of those with a d_{XRD} of 5.7 and 6.5 nm, probably due to their <1 nm difference in average size and partial overlapping in their particle size distributions (Supporting Information, Figure S1).

Accordingly, when the particle mass concentration of each nanoparticle is adjusted to the same surface area concentration (340 m^2/L, filled symbols in Figure 2b) all samples yield comparable values. Only the largest CeO_2 nanoparticles (filled inverse triangles in Figure 2b) decomposed a lower amount of H_2O_2. This may be attributed to the substantially higher mass concentration (3.96 g/L) required to achieve the desired surface area concentration of 340 m^2/L, that results in particle agglomeration (Supporting Information, Figure S5) reducing their effective surface area concentration in suspension, and/or due to potential surface differences of the largest sample that might have fewer surface defects. Nonetheless, the high correlation of the CAT-mimetic activity to the surface area concentration indicates that the catalytic activity of nano-CeO_2:Eu^{3+} is a surface phenomenon and further agrees with the reported higher antioxidant capacity of smaller nanoparticles compared to the larger ones.[23,25] In agreement with the literature,[42] the CAT-mimetic activity of CeO_2:Eu^{3+} is unaffected by rare-earth doping for Eu-content up to 5 at% (Supporting Information, Figure S6). However, it cannot be excluded that higher doping contents might eventually affect the catalytic activity.

As described earlier, the emission luminescence of CeO_2:Eu^{3+} upon UV excitation strongly depends on the Ce−O charge transfer.[39] So any charge redistribution on the Ce−O bond resulting from the H_2O_2 interaction should affect the emission luminescence.[38] However, it has been established that addition of H_2O_2 increases the Ce−O coordination number (Ce−O bond length)[24] resulting in a delocalized redistribution of charge density.[25] Indeed, Figure 2c shows the emission spectra (excitation λ = 330 nm) of the smallest CeO_2:Eu^{3+} (d_{XRD} = 4.4 nm) dispersed in aqueous solution (0.5 g/L) before (red lines) and after H_2O_2 addition (blue lines, 4 mM). As soon as the H_2O_2 is added, the signal intensity is almost completely quenched. Thus, the mechanism of this CeO_2:Eu^{3+} luminescent quenching is the charge redistribution[25] and increased Ce−O coordination number[24] upon H_2O_2-nanoparticle interactions.

Label-free H_2O_2 Sensing in Biological Media. Due to the distinct luminescence quenching of the nano-CeO_2:Eu^{3+} in the presence of H_2O_2, these nanoparticles could be employed as H_2O_2 biosensors by monitoring their emission intensity at λ = 590 nm. The sensor response is defined as $1-I_s/I_0$, where I_s is the emission intensity in the presence of H_2O_2 and I_0 that in the absence of H_2O_2. While 5 at% Eu displays the highest

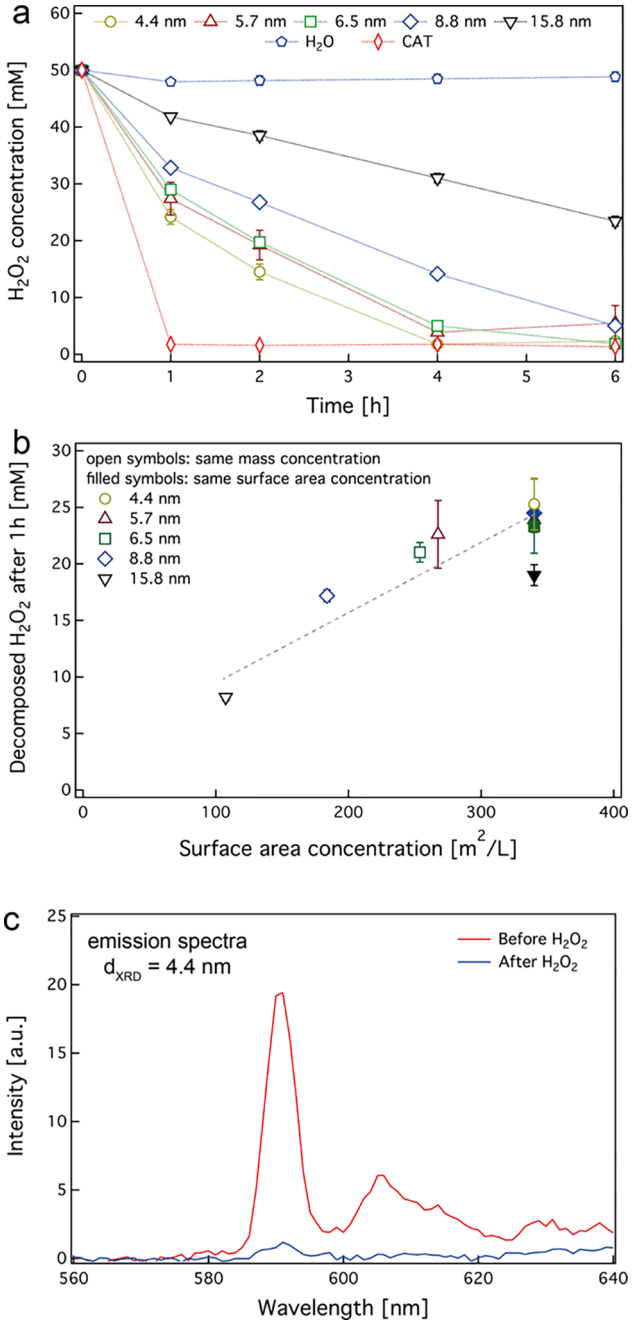

Figure 2. CAT-mimetic catalytic H_2O_2 decomposition. (a) CAT-mimetic activity of all CeO_2:Eu^{3+} nanoparticles here monitoring the H_2O_2 decomposition over time and compared to the activity of CAT (red diamonds) and pure water (blue hexagons). Smaller nanoparticles exhibit higher activity, indicating a surface area related phenomenon. (b) The decomposed H_2O_2 concentration after 1 h incubation with all nanoparticles for the same surface area concentration (filled symbols) and same mass concentration in solution (open symbols). The CAT-mimetic activity of all nanoparticles here follow the same trend when expressed as a function of surface area concentration. Only the largest nanoparticles exhibit a slightly lower H_2O_2 decomposition, which may be attributed to particle agglomeration due to the high mass concentration needed to achieve the desired surface area concentration, reducing their effective surface area. Mean ± standard deviation (S.D., N = 4−6). (c) Emission spectra of the smallest (d_{XRD} = 4.4 nm) CeO_2:Eu^{3+} nanoparticles as in (a) solutions before (red line) and after H_2O_2 addition (blue line).

DOI: 10.1021/acsnano.7b05518
ACS Nano 2017, 11, 12210−12218

sensor response for H_2O_2, it should be noted that lower Eu-contents (0.1 and 1 at%) also exhibit a sensor response (Supporting Information, Figure S7). Figure 3a shows the sensor response of all nano-CeO_2:Eu^{3+} with 5 atom % Eu dispersed in an aqueous solution as a function of SSA for two H_2O_2 concentrations C = 50 (filled symbols) and 500 μM (open symbols), following particle concentration optimization (see Supporting Information, Figure S8). The sensor response increases for higher SSA (and thus lower nanoparticle size) for both H_2O_2 concentrations, further highlighting the size dependent luminescence quenching, with the smallest nanoparticles exhibiting the highest sensor response at the same mass concentration. This is in agreement with a recent report describing the MoS_2 particle size dependent response to H_2O_2 by electrochemical sensing, which was explained by increasing sulfur deficiency of the smaller particles.[8] The H_2O_2 - nanoparticle reaction is manifested by a clear substrate dependent luminescence quenching in the emission spectrum of CeO_2:Eu^{3+} nanoparticles subjected to increasing H_2O_2 concentrations (Supporting Information, Figure S9). Furthermore, the particle luminescence is almost completely quenched with the smallest CeO_2:Eu^{3+} nanoparticles at elevated H_2O_2 concentration (Figures 2c and 3a), suggesting that further size reduction may not notably impact the catalytic properties at these conditions.

The smallest CeO_2:Eu^{3+} nanoparticles here (d_{XRD} = 4.4 nm) are further characterized with the aim to develop a highly sensitive H_2O_2 biosensor functional in physiologically relevant solutions. The sensor response for H_2O_2 concentrations ranging from 0.05 to 500 μM is assayed in phosphate buffered saline (PBS) and is linear up to 2.5 μM H_2O_2 with an LOD and limit-of-quantification (LOQ) of 0.15 μM and 0.46 μM, respectively (Figure 3b,c). A saturation is reached for >100 μM H_2O_2 concentrations. When the concentration and sensor response reciprocals are plotted, a broader linear range can be detected (Figure 3b, inset), yielding a Michaelis Menten constant K_M of 4.3 μM for the nano-CeO_2:Eu^{3+} studied here. Similar results were obtained in pure water as well as in potassium phosphate (KPi) buffer (Supporting Information, Figure S10). The here developed biosensor is not affected by the presence of several ions (*e.g.*, Na^+, K^+, Cl^-, PO_4^{3-}) in PBS at high concentrations. The luminescence quenching of CeO_2:Eu^{3+} in the presence of several compounds is studied (Supporting Information, Figure S11). Even though the CeO_2:Eu^{3+} nanoparticles are functional in the presence of proteins (serum) as well as neutral and negatively charged amino acids, interference is observed in the presence of positively charged amino acids (arginine, histidine and lysine), elevated ion concentrations ($MgSO_4$, $Fe(NO_3)_3$) and anti-oxidants (uric acid, ascorbic acid). This interference does not inhibit the employment of the here developed H_2O_2 biosensors as a tool for sensitive detection either of H_2O_2 in cell culture media (*e.g.*, production of H_2O_2 from cells), or linked to enzyme-coupled reactions in buffered solutions containing proteins for the detection of bioanalytes, as it will be shown later on.

The CeO_2:Eu^{3+} nanoparticles here demonstrate superior stability when compared to commonly employed H_2O_2 sensitive dyes, which exhibit poor stability even at ambient conditions, mainly due to photobleaching (Supporting Information, Figure S12a). In addition, the low LOD achieved here by the smallest nano-CeO_2:Eu^{3+} outperforms all reported optical, particle-based, enzyme-, conjugate- and label-free

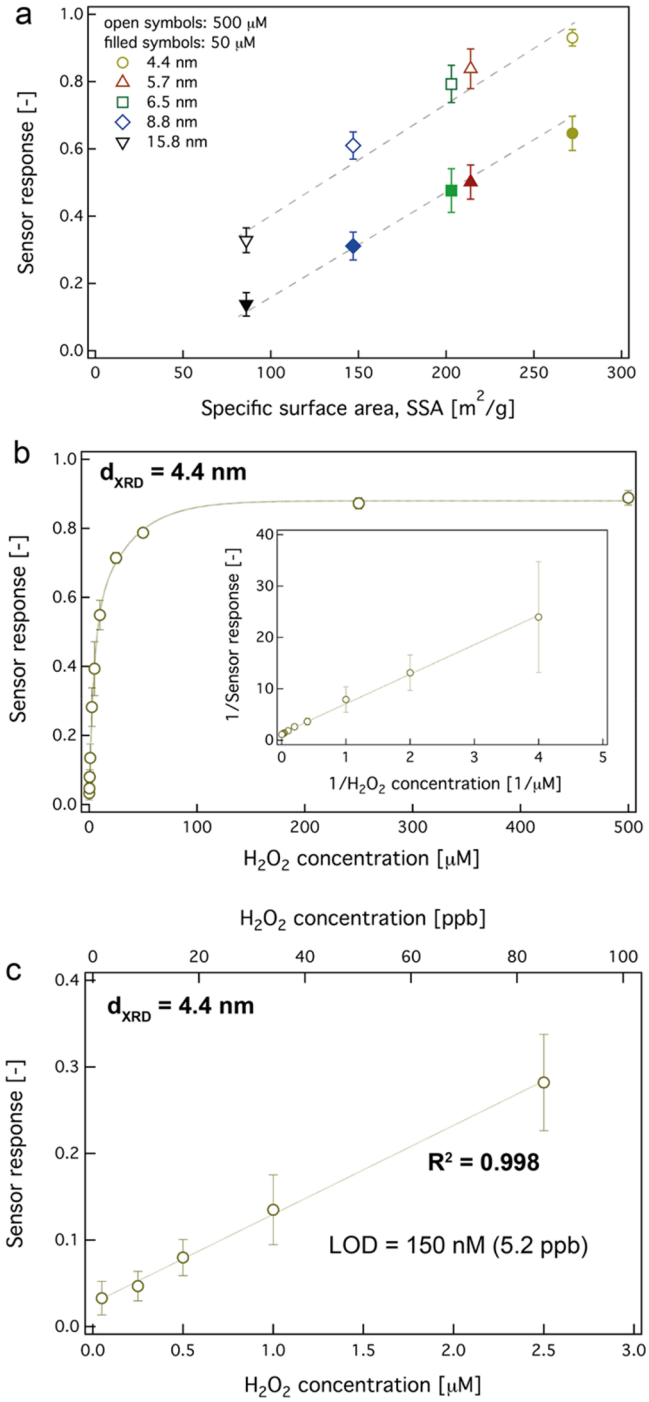

Figure 3. Label-free phosphorescent H_2O_2 biosensing. (a) Calculated sensor response ($1-I_s/I_0$) for two different H_2O_2 concentrations (open symbols: 500 μM, filled symbols: 50 μM) as a function of SSA reveals a linear dependency, indicating highest sensitivity for the smallest nanoparticles. (b) The sensor response of the smallest nanoparticle (d_{XRD} = 4.4 nm) is depicted for increasing concentrations of H_2O_2 (0.05−500 μM) in PBS. As inset, the concentration and sensor response reciprocals are plotted (0.25−500 μM H_2O_2) revealing a large linear range and a K_M = 4.3 μM. (c) Linear range of sensor response as a function of H_2O_2 in PBS (0.05−2.5 μM) with an LOD and LOQ of 0.15 and 0.46 μM H_2O_2, respectively. Mean ± S.D. (N = 3).

approaches for H_2O_2 detection in physiological conditions, highlighting their superior performance. Emission quenching is slowly reversible (Supporting Information, Figure S12b) and

DOI: 10.1021/acsnano.7b05518
ACS Nano 2017, 11, 12210−12218

Table 1. Particle-Based Approaches for the Enzyme-, Conjugate-, and Organic Dye-Free Fluorimetric Detection of H_2O_2 in Physiological Fluids[a]

material	description	LOD (μM)	reference
CdTe	quantum dots	1.00	13
CdTe/CdS	quantum dots, core/shell	1.80	5
polymer/Eu^{3+}	poly(methyl methacrylate) nanoparticles (100−200 nm) with Eu^{3+} complex	2.00	10
Fe_3O_4−CdTe	nanocomposite quantum dots, core/shell (primary particle ∼30 nm)	35.0	14
$CePO_4$:Tb^{3+}	nanoneedles (5 nm × 100 nm)	1.03	11
polymer/Tb^{3+}	coordination polymer nanoparticles (670 nm) with Tb^{3+} complex	2.00	12
YVO_4:Eu^{3+}	nanoparticles (20−40 nm)	1.50	9
CeO_2:Eu^{3+}	nanoparticles (4.4 nm)	0.15	this work

[a]The rationally-designed biomimetic enzyme-like CeO_2:Eu^{3+} nanoparticles exhibit the lowest LOD in comparison to all materials listed in the literature.

further studies of CeO_2:Eu^{3+} nanoparticles with H_2O_2 are needed to better understand this interaction. Furthermore, the high reproducibility of this nanomanufacture process is highlighted by the almost identical sensor response obtained with different particle batches (Supporting Information, Figure S12c). The improved sensitivity here may be further supported by the predominant Ce^{4+} (Supporting Information, Figure S4), according to a recent report demonstrating the correlation of increased magnitude of response with Ce^{4+}:Ce^{3+} ratio.[31] Table 1 summarizes reported literature on such biosensors, listing the corresponding particle composition and size. The superiority of the current developed sensor is attributed both to the significantly smaller size (4.4 nm) in comparison to most other phosphor-based nanoparticles with sizes >20 nm and the high particle reactivity.

Alcohol Oxidase-Coupled Alcohol Sensing. Capitalizing on the demonstrated H_2O_2 biosensing, the application of CeO_2:Eu^{3+} nanoparticles is extended to ethanol sensing. Ethanol is oxidized to acetaldehyde and H_2O_2 in the presence of AOx, which leads to quenching of CeO_2:Eu^{3+} luminescence. The sensor response for ethanol in PBS is linear in the millimolar range as illustrated in Figure 4a. The obtained sensitivity range for ethanol is comparable to detection by gas chromatography, where ethanol concentrations greater than 0.01 g/dL (2.2 mM) are reported.[43] The average accuracy to determine a spiked sample containing 6 mM ethanol is acceptable at 104%. This demonstrates a proof of principle of how CeO_2:Eu^{3+} nanoparticles can be adopted to extend their application to further metabolites. The described assay here may present an alternative ethanol sensor to gas chromatography as it is inexpensive, fast and does not require sophisticated expertise. Ethanol can also be measured in the presence of proteins (Supporting Information, Figure S13), however further optimizations would be necessary to improve the dynamic range and sensitivity to allow routine measurements in plasma and other bodily fluids.

Furthermore, it is well established that AOx possesses a reduced substrate selectivity allowing oxidation of various short chain alcohols.[44] In a subsequent step the AOx-coupled sensor response for primary alcohols of differing chain length and branching is investigated at a concentration of 12.5 mM. Figure 4b shows that the sensor response is inversely correlated to chain length and is substantially dampened for branched alcohols such as isopropanol.[45] This further validates the potential of enzyme-mimetic antioxidant luminescent CeO_2:Eu^{3+} nanoparticles for the detection of biologically relevant metabolites.

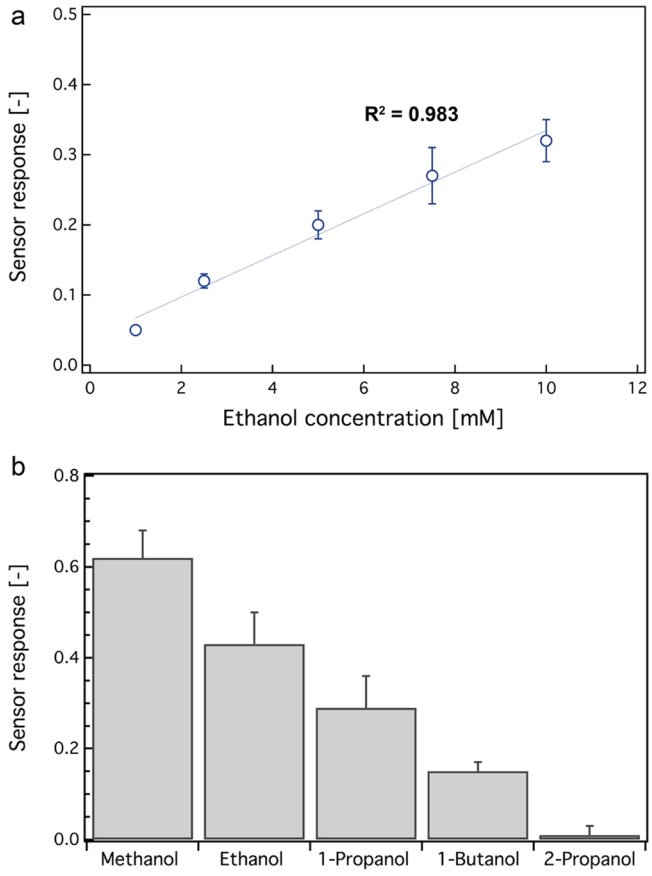

Figure 4. Alcohol oxidase-coupled alcohol sensing. (a) The linear range of the sensor response for ethanol (1−10 mM) detection mediated by AOx (0.05 μg/mL) using the smallest nanoparticle (d_{XRD} = 4.4 nm). This demonstrates the potential of CeO_2:Eu^{3+} to detect additional biologically relevant metabolites. (b) Sensor selectivity for alcohols (12.5 mM) of varying chain length and branching exhibits highest sensor response for short chain aliphatic alcohols. Mean + S.D. (N = 3).

CONCLUSIONS

We show here how enzyme-mimetic nanoparticles can be engineered to render them highly sensitive H_2O_2 sensors in biological assay solutions for analytical detection in media with or without proteins. Capitalizing on the biomimetic antioxidant activity of CeO_2 nanoparticles, we systematically vary their size and link their CAT-mimetic activity to their surface area concentration in solution. The observed SSA-dependent activity of these nanoparticles excludes a particle bulk effect,

DOI: 10.1021/acsnano.7b05518
ACS Nano 2017, 11, 12210−12218

and in fact, it is shown that CeO_2-based nanoparticles with the same surface area concentration in solution exhibit similar CAT-mimetic activity. A rare-earth dopant (Eu^{3+}) introduced during nanoparticle synthesis increases the particle luminescence, which is quenched upon H_2O_2 interaction with the CeO_2 surface. The strong surface area dependency of both the CAT-mimetic activity and the H_2O_2 biosensing performance highlights that these phenomena are surface-related, with the highest sensor response detected with the smallest nanoparticles. Furthermore, luminescence quenching is H_2O_2 concentration dependent, rendering the CeO_2:Eu^{3+} nanoparticles highly sensitive enzyme-, conjugate-, and organic dye-free H_2O_2 biosensors with an LOD down to 0.15 μM (5.2 ppb), outperforming reported particle-based fluorimetric approaches and exhibiting higher stability than commonly used fluorescent organic dyes. Doping with rare-earth ions active in the near-infrared region[46] may enable H_2O_2 detection *in vivo* in future studies, though efforts should be made to increase the substrate selectivity, to limit the interference stemming from intersubject variable metabolite levels. When coupled with AOx, an ethanol concentration dependent sensor response is obtained. This highlights the potential of enzyme-mimetic antioxidant luminescent CeO_2:Eu^{3+} nanoparticles in future sophisticated *in vitro* assays and devices for the detection of disease biomarkers.

METHODS

Particle Synthesis and Characterization. The CeO_2 nanoparticles containing 5 at% Europium were prepared by FSP of a liquid precursor solution containing 0.1−0.3 M Cerium 2-ethylhexanoate (98%, Strem) and appropriate amount of Eu-nitrate (99.9%, Sigma-Aldrich) dissolved in a 1:1 ratio of 2-ethylhexanoic acid (>99%, Sigma-Aldrich) and ethanol (>99.8%, Fluka). The liquid precursor solution was fed through the FSP nozzle with the aid of a syringe pump (Lambda) at a flow rate of 3−8 mL/min and dispersed into a fine spray with O_2 (>99.5%, PanGas) at flow rate 3−8 L/min. The spray was ignited with a premixed methane/O_2 (>99.5%, PanGas) flame. The particle size was controlled by tuning the Ce-precursor concentration within the flame as defined below (eq 1), where mol_{Ce}/min is the molecular flow rate of Ce atoms and L_{o_2}disp/min is the O_2 dispersion gas volume flow rate. The as-produced nanoparticles were collected on a GF 6 257 glass fiber filter (Hahnemühle FineArt GmbH) with the aid of an MM1 104 BV vacuum pump (Busch Mink).

$$\text{Precursor concentration} = \frac{\text{mol}_{Ce}/\text{min}}{L_{O_2\text{disp}}/\text{min}} \quad (1)$$

The crystallinity of the collected nanoparticles was examined on an AXS D8 diffractometer (Bruker) at a scan rate 7.9°/min. The average crystal sizes were determined with Rietveld refinement using the TOPAS4 software (Bruker). N_2 adsorption was performed on a TriStar surface area and porosity system (Micromeritics) at −196 °C after degassing the samples at 150 °C for at least 1 h. High-resolution TEM images were acquired on a Tecnai F30 microscope (FEI) operated at V_{acc} = 300 kV. X-ray photoelectron spectroscopy was performed on a K-Alpha$^+$ XPS spectrometer (Thermo Scientific). All samples were compacted to form flakes prior to analysis and high-resolution spectra acquired to investigate the chemical states present. All data were acquired, processed, and exported from the Avantage software (Thermo Scientific). The hydrodynamic diameter and zeta potential were determined using a DelsaNano C particle size analyzer (Beckman Coulter) or a 3D DLS (LS Technologies).

Catalytic H_2O_2 Decomposition. The CeO_2:Eu^{3+} nanoparticles (d_{XRD} = 4.4−15.8 nm) were dispersed in Milli-Q water by vortexing and sonication (RK 31 H, Sonorex) and incubated with 50 mM H_2O_2 at a particle mass concentration of 1.25 g/L or surface area concentration of 340 m^2/L and rotated for up to 6 h at room temperature (RT). CAT from bovine liver (≥30'000 U/mg, Sigma-Aldrich) was assayed at a final concentration of 0.5 mg/L. Aliquots were sampled at selected time points and particles removed by centrifugation (10 min, 15 000*g*) or CAT inactivated by heat (5 min, 95 °C). Samples were assayed at 240 nm using an M200 infinite plate reader (Tecan).

Phosphorescence Characterization and H_2O_2 Sensing. Excitation (250−450 nm) and emission (550−700 nm) spectra were recorded using a Cary Eclipse fluorescence spectrophotometer (Agilent). All CeO_2:Eu^{3+} nanoparticles (d_{XRD} = 4.4−15.8 nm) were assayed in the powder form using a powder holder following manual compaction. Smallest nanoceria (d_{XRD} = 4.4 nm) spectra were additionally collected in the aqueous phase using a microplate holder accessory in the absence or presence of H_2O_2 either at 4 mM or titrated from 0.5 to 1000 μM, at a particle mass concentration of 0.5 g/L or 0.125 g/L, respectively. An overview of all applied parameters is given in Table S2.

For all sensing experiments, particles (d_{XRD} = 4.4 nm) were dispersed in Milli-Q water. Samples and H_2O_2 standards were prepared in 100 mM KPi pH 7.4, PBS, composed of 137 mM sodium chloride, 2.7 mM potassium chloride, 10 mM disodium phosphate, and 18 mM monopotassium phosphate or 10% FBS supplemented DMEM (Thermo Fischer Scientific). Particles (0.125 g/L) were added to samples (0−500 μM H_2O_2) and kept at RT for 30 min prior to measurement by phosphorescence (λ_{ex} = 330 nm, λ_{em} = 590 nm). Upon the dispersion of the particles in solutions they settle on the bottom of the wells typically within 30 min[47] and this is why the sensor response is measured at least after 30 min from H_2O_2 addition. A blank reference sample, free of H_2O_2 was included in each measurement to determine the sensor response. LOD and LOQ were computed in Excel derived from the standard deviation of the sensor response (Sy) and the slope (m). LOD and LOQ were defined as 3.3 × Sy/m and 10 × Sy/m, respectively.

To follow the emission over time, particles were rotated and briefly sonicated at selected time points prior to recording phosphorescence. The sensor response for 2 μM and 50 μM H_2O_2 was assayed with two different particle batches (0.125 g/L). To compare the stability of the here described particles to a commercially available H_2O_2 sensitive probe, Amplex Ultra Red (AUR, Thermo Fischer Scientific) was applied in a horseradish peroxidase (HRP, ≥ 225 U/mg, Sigma-Aldrich) coupled reaction. H_2O_2 was assayed from 0.05−10 μM in 100 mM KPi, pH 7.4 with 50 μM AUR and 1 U/mL HRP, and the signal acquired by fluorescence (λ_{ex} = 490 nm, λ_{em} = 585 nm) using an M200 infinite plate reader (Tecan). CeO_2:Eu^{3+} particles and AUR/HRP were kept for 8 h at RT, unprotected from light and the signal intensity for 2 μM H_2O_2 monitored at selected time points. Sample accuracy was determined by dividing the measured value over the nominal, expressed in percentage.

Alcohol Oxidase-Coupled Alcohol Sensing. Ethanol standards and alcohol samples, including methanol, ethanol, 1-propanol, 1-butanol, and 2-propanol, were incubated with AOx from *P. Pastoris* (10−40 U/mg, Sigma-Aldrich) in PBS or 10% FBS, PBS for 30 min at RT prior to adding CeO_2:Eu^{3+} nanoparticles dispersed in Milli-Q water. The phosphorescence intensity after 30 min was recorded as described for H_2O_2 sensing. The sensor response of ethanol standards was referenced to a blank sample free of ethanol containing AOx. Alcohol samples were incubated accordingly with AOx for the alcohol sensor selectivity assay. Ethanol standards, spiked ethanol sample, and alcohols were assayed at a final concentration of 1−10 mM or 5−20 mM, 6 mM, and 12.5 mM, respectively, with 0.05 μg/mL AOx.

ASSOCIATED CONTENT

Supporting Information

The Supporting Information is available free of charge on the ACS Publications website at DOI: 10.1021/acsnano.7b05518.

Experimental details, additional figures and tables as described in the text (PDF)

DOI: 10.1021/acsnano.7b05518
ACS Nano 2017, 11, 12210−12218

AUTHOR INFORMATION

Corresponding Author

*georgios.sotiriou@ki.se.

ORCID

Georgios A. Sotiriou: 0000-0001-5040-620X

Notes

The authors declare no competing financial interest.

ACKNOWLEDGMENTS

The authors thank Dr. Deeks (Thermo Fisher Scientific) for the XPS measurements and Prof. Pratsinis (ETH Zurich) for access to FSP facilities and characterization instruments. TEM was performed at ScopeM, the imaging center of ETH Zurich. Anna Pratsinis acknowledges financial support from an ETH research grant (ETH-10 13-1). Georgios A. Sotiriou acknowledges the Swiss National Science Foundation for an Advanced Researcher fellowship (PA00P2 145392) and funding from the Karolinska Institutet Board of Research, the Swedish Research Council (2016-03471), the Jeansson Foundations (JS2016-0029), and the Åke Wiberg Foundation (M16-0098).

REFERENCES

(1) Walkey, C.; Das, S.; Seal, S.; Erlichman, J.; Heckman, K.; Ghibelli, L.; Traversa, E.; McGinnis, J. F.; Self, W. T. Catalytic Properties and Biomedical Applications of Cerium Oxide Nanoparticles. *Environ. Sci.: Nano* **2015**, *2*, 33−53.

(2) Puertollano, M. A.; Puertollano, E.; de Cienfuegos, G. A.; de Pablo, M. A. Dietary Antioxidants: Immunity and Host Defense. *Curr. Top. Med. Chem.* **2011**, *11*, 1752−1766.

(3) Halliwell, B.; Clement, M. V.; Long, L. H. Hydrogen Peroxide in the Human Body. *FEBS Lett.* **2000**, *486*, 10−13.

(4) de la Rica, R.; Stevens, M. M. Plasmonic ELISA for the Ultrasensitive Detection of Disease Biomarkers with the Naked Eye. *Nat. Nanotechnol.* **2012**, *7*, 821−824.

(5) Hu, M.; Tian, J.; Lu, H. T.; Weng, L. X.; Wang, L. H. H_2O_2-Sensitive Quantum Dots for the Label-Free Detection of Glucose. *Talanta* **2010**, *82*, 997−1002.

(6) Liu, B. W.; Sun, Z. Y.; Huang, P. J. J.; Liu, J. W. Hydrogen Peroxide Displacing DNA from Nanoceria: Mechanism and Detection of Glucose in Serum. *J. Am. Chem. Soc.* **2015**, *137*, 1290−1295.

(7) Azevedo, A. M.; Prazeres, D. M. F.; Cabral, J. M. S.; Fonseca, L. P. Ethanol Biosensors Based on Alcohol Oxidase. *Biosens. Bioelectron.* **2005**, *21*, 235−247.

(8) Gupta, A.; Rawal, T. B.; Neal, C. J.; Das, S.; Rahman, T. S.; Seal, S. Molybdenum Disulfide for Ultra-Low Detection of Free Radicals: Electrochemical Response and Molecular Modeling. *2D Mater.* **2017**, *4*, 025077.

(9) Duee, N.; Ambard, C.; Pereira, F.; Portehault, D.; Viana, B.; Valle, K.; Autissier, D.; Sanchez, C. New Synthesis Strategies for Luminescent YVO_4:Eu and $EuVO_4$ Nanoparticles with H_2O_2 Selective Sensing Properties. *Chem. Mater.* **2015**, *27*, 5198−5205.

(10) Li, Z. J.; Zhang, H. W.; Shen, J. S. Preparation of Stable Luminescent Poly(Methyl Methacrylate)-Europium Complex Nanospheres and Application in the Detection of Hydrogen Peroxide with the Biocatalytic Growth of Gold Nanoparticles. *J. Appl. Polym. Sci.* **2013**, *128*, 845−850.

(11) Lv, C. J.; Di, W. H.; Liu, Z. H.; Zheng, K. Z.; Qin, W. P. Luminescent $Cepo_4$: Tb Colloids for H_2O_2 and Glucose Sensing. *Analyst* **2014**, *139*, 4547−4555.

(12) Tan, H. L.; Ma, C. J.; Li, Q.; Wang, L.; Xu, F. G.; Chen, S. H.; Song, Y. H. Functionalized Lanthanide Coordination Polymer Nanoparticles for Selective Sensing of Hydrogen Peroxide in Biological Fluids. *Analyst* **2014**, *139*, 5516−5522.

(13) Yuan, J. P.; Guo, W. W.; Yin, J. Y.; Wang, E. K. Glutathione-Capped CdTe Quantum Dots for the Sensitive Detection of Glucose. *Talanta* **2009**, *77*, 1858−1863.

(14) Zheng, H.; Su, R. X.; Gao, Z.; Qi, W.; Huang, R. L.; Wang, L. B.; He, Z. M. Magnetic-Fluorescent Nanocomposites as Reusable Fluorescence Probes for Sensitive Detection of Hydrogen Peroxide and Glucose. *Anal. Methods* **2014**, *6*, 6352−6357.

(15) Burmistrova, N. A.; Kolontaeva, O. A.; Duerkop, A. New Nanomaterials and Luminescent Optical Sensors for Detection of Hydrogen Peroxide. *Chemosensors* **2015**, *3*, 253−273.

(16) Stone, J. R.; Yang, S. P. Hydrogen Peroxide: A Signaling Messenger. *Antioxid. Redox Signaling* **2006**, *8*, 243−270.

(17) Wei, H.; Wang, E. K. Nanomaterials with Enzyme-Like Characteristics (Nanozymes): Next-Generation Artificial Enzymes. *Chem. Soc. Rev.* **2013**, *42*, 6060−6093.

(18) Lin, Y. H.; Ren, J. S.; Qu, X. G. Catalytically Active Nanomaterials: A Promising Candidate for Artificial Enzymes. *Acc. Chem. Res.* **2014**, *47*, 1097−1105.

(19) Heckman, K. L.; DeCoteau, W.; Estevez, A.; Reed, K. J.; Costanzo, W.; Sanford, D.; Leiter, J. C.; Clauss, J.; Knapp, K.; Gomez, C.; Mullen, P.; Rathbun, E.; Prime, K.; Marini, J.; Patchefsky, J.; Patchefsky, A. S.; Hailstone, R. K.; Erlichman, J. S. Custom Cerium Oxide Nanoparticles Protect against a Free Radical Mediated Autoimmune Degenerative Disease in the Brain. *ACS Nano* **2013**, *7*, 10582−10596.

(20) Grulke, E.; Reed, K.; Beck, M.; Huang, X.; Cormack, A.; Seal, S. Nanoceria: Factors Affecting Its Pro- and Anti-Oxidant Properties. *Environ. Sci.: Nano* **2014**, *1*, 429−444.

(21) Gupta, A.; Das, S.; Neal, C. J.; Seal, S. Controlling the Surface Chemistry of Cerium Oxide Nanoparticles for Biological Applications. *J. Mater. Chem. B* **2016**, *4*, 3195−3202.

(22) Li, Y. Y.; He, X.; Yin, J. J.; Ma, Y. H.; Zhang, P.; Li, J. Y.; Ding, Y. Y.; Zhang, J.; Zhao, Y. L.; Chai, Z. F.; Zhang, Z. Y. Acquired Superoxide-Scavenging Ability of Ceria Nanoparticles. *Angew. Chem., Int. Ed.* **2015**, *54*, 1832−1835.

(23) Lee, S. S.; Song, W. S.; Cho, M. J.; Puppala, H. L.; Nguyen, P.; Zhu, H. G.; Segatori, L.; Colvin, V. L. Antioxidant Properties of Cerium Oxide Nanocrystals as a Function of Nanocrystal Diameter and Surface Coating. *ACS Nano* **2013**, *7*, 9693−9703.

(24) Wang, Y. J.; Dong, H.; Lyu, G. M.; Zhang, H. Y.; Ke, J.; Kang, L. Q.; Teng, J. L.; Sun, L. D.; Si, R.; Zhang, J.; Liu, Y. J.; Zhang, Y. W.; Huang, Y. H.; Yan, C. H. Engineering the Defect State and Reducibility of Ceria Based Nanoparticles for Improved Anti-Oxidation Performance. *Nanoscale* **2015**, *7*, 13981−13990.

(25) Cafun, J. D.; Kvashnina, K. O.; Casals, E.; Puntes, V. F.; Glatzel, P. Absence of Ce^{3+} Sites in Chemically Active Colloidal Ceria Nanoparticles. *ACS Nano* **2013**, *7*, 10726−10732.

(26) Chen, Z. W.; Yin, J. J.; Zhou, Y. T.; Zhang, Y.; Song, L.; Song, M. J.; Hu, S. L.; Gu, N. Dual Enzyme-Like Activities of Iron Oxide Nanoparticles and Their Implication for Diminishing Cytotoxicity. *ACS Nano* **2012**, *6*, 4001−4012.

(27) Chen, J. P.; Patil, S.; Seal, S.; McGinnis, J. F. Rare Earth Nanoparticles Prevent Retinal Degeneration Induced by Intracellular Peroxides. *Nat. Nanotechnol.* **2006**, *1*, 142−150.

(28) Das, M.; Patil, S.; Bhargava, N.; Kang, J. F.; Riedel, L. M.; Seal, S.; Hickman, J. J. Auto-Catalytic Ceria Nanoparticles Offer Neuroprotection to Adult Rat Spinal Cord Neurons. *Biomaterials* **2007**, *28*, 1918−1925.

(29) Singh, R.; Karakoti, A. S.; Self, W.; Seal, S.; Singh, S. Redox-Sensitive Cerium Oxide Nanoparticles Protect Human Keratinocytes from Oxidative Stress Induced by Glutathione Depletion. *Langmuir* **2016**, *32*, 12202−12211.

(30) Mehta, A.; Patil, S.; Bang, H.; Cho, H. J.; Seal, S. A Novel Multivalent Nanomaterial Based Hydrogen Peroxide Sensor. *Sens. Actuators, A* **2007**, *134*, 146−151.

(31) Neal, C. J.; Gupta, A.; Barkam, S.; Saraf, S.; Das, S.; Cho, H. J.; Seal, S. Picomolar Detection of Hydrogen Peroxide Using Enzyme-Free Inorganic Nanoparticle-Based Sensor. *Sci. Rep.* **2017**, *7*, 1324.

(32) Pratsinis, S. E. Aerosol-Based Technologies in Nanoscale Manufacturing: From Functional Materials to Devices through Core Chemical Engineering. *AIChE J.* **2010**, *56*, 3028−3035.

DOI: 10.1021/acsnano.7b05518
ACS Nano 2017, 11, 12210−12218

(33) Madler, L.; Stark, W. J.; Pratsinis, S. E. Flame-Made Ceria Nanoparticles. *J. Mater. Res.* **2002**, *17*, 1356−1362.
(34) Sotiriou, G. A.; Schneider, M.; Pratsinis, S. E. Color-Tunable Nanophosphors by Codoping Flame-Made Y_2O_3 with Tb and Eu. *J. Phys. Chem. C* **2011**, *115*, 1084−1089.
(35) Gass, S.; Cohen, J. M.; Pyrgiotakis, G.; Sotiriou, G. A.; Pratsinis, S. E.; Demokritou, P. Safer Formulation Concept for Flame-Generated Engineered Nanomaterials. *ACS Sustainable Chem. Eng.* **2013**, *1*, 843−857.
(36) Gulicovski, J. J.; Bracko, I.; Milonjic, S. K. Morphology and the Isoelectric Point of Nanosized Aqueous Ceria Sols. *Mater. Chem. Phys.* **2014**, *148*, 868−873.
(37) Xia, T.; Kovochich, M.; Liong, M.; Madler, L.; Gilbert, B.; Shi, H. B.; Yeh, J. I.; Zink, J. I.; Nel, A. E. Comparison of the Mechanism of Toxicity of Zinc Oxide and Cerium Oxide Nanoparticles Based on Dissolution and Oxidative Stress Properties. *ACS Nano* **2008**, *2*, 2121−2134.
(38) Li, L.; Yang, H. K.; Moon, B. K.; Fu, Z. L.; Guo, C. F.; Jeong, J. H.; Yi, S. S.; Jang, K.; Lee, H. S. Photoluminescence Properties of CeO_2:Eu^{3+} Nanoparticles Synthesized by a Sol-Gel Method. *J. Phys. Chem. C* **2009**, *113*, 610−617.
(39) Kumar, A.; Babu, S.; Karakoti, A. S.; Schulte, A.; Seal, S. Luminescence Properties of Europium-Doped Cerium Oxide Nanoparticles: Role of Vacancy and Oxidation States. *Langmuir* **2009**, *25*, 10998−11007.
(40) Sotiriou, G. A.; Schneider, M.; Pratsinis, S. E. Green, Silica-Coated Monoclinic Y_2O_3:Tb^{3+} Nanophosphors: Flame Synthesis and Characterization. *J. Phys. Chem. C* **2012**, *116*, 4493−4499.
(41) Pirmohamed, T.; Dowding, J. M.; Singh, S.; Wasserman, B.; Heckert, E.; Karakoti, A. S.; King, J. E. S.; Seal, S.; Self, W. T. Nanoceria Exhibit Redox State-Dependent Catalase Mimetic Activity. *Chem. Commun.* **2010**, *46*, 2736−2738.
(42) Babu, S.; Cho, J. H.; Dowding, J. M.; Heckert, E.; Komanski, C.; Das, S.; Colon, J.; Baker, C. H.; Bass, M.; Self, W. T.; Seal, S. Multicolored Redox Active Upconverter Cerium Oxide Nanoparticle for Bio-Imaging and Therapeutics. *Chem. Commun.* **2010**, *46*, 6915−6917.
(43) Tiscione, N. B.; Alford, I.; Yeatman, D. T.; Shan, X. Q. Ethanol Analysis by Headspace Gas Chromatography with Simultaneous Flame-Ionization and Mass Spectrometry Detection. *J. Anal. Toxicol.* **2011**, *35*, 501−511.
(44) Gulce, H.; Gulce, A.; Kavanoz, M.; Coskun, H.; Yildiz, A. A New Amperometric Enzyme Electrode for Alcohol Determination. *Biosens. Bioelectron.* **2002**, *17*, 517−521.
(45) Koch, C.; Neumann, P.; Valerius, O.; Feussner, I.; Ficner, R. Crystal Structure of Alcohol Oxidase from Pichia Pastoris. *PLoS One* **2016**, *11*, e0149846.
(46) Chen, G. Y.; Ohulchanskyy, T. Y.; Liu, S.; Law, W. C.; Wu, F.; Swihart, M. T.; Agren, H.; Prasad, P. N. Core/Shell $NaGdF_4$:Nd^{3+}/$NaGdF_4$ Nanocrystals with Efficient near-Infrared to near-Infrared Downconversion Photoluminescence for Bioimaging Applications. *ACS Nano* **2012**, *6*, 2969−2977.
(47) Spyrogianni, A.; Herrmann, I. K.; Lucas, M. S.; Leroux, J. C.; Sotiriou, G. A. Quantitative Analysis of the Deposited Nanoparticle Dose on Cell Cultures by Optical Absorption Spectroscopy. *Nanomedicine* **2016**, *11*, 2483−2496.

DOI: 10.1021/acsnano.7b05518
ACS Nano 2017, 11, 12210−12218